frontiers | Frontiers in Bioengineering and Biotechnology

TYPE Original Research
PUBLISHED 23 March 2023
DOI 10.3389/fbioe.2023.1168750

OPEN ACCESS

EDITED BY
Xiangzhao Ai,
Shanghai Jiao Tong University, China

REVIEWED BY
Liu Ying Xiang,
Fourth Military Medical University, China
Zhuo Wang,
Fudan University, China

*CORRESPONDENCE
Guannan Wang,
chemwangguannan@gmail.com

†These authors have contributed equally to this work

SPECIALTY SECTION
This article was submitted to Nanobiotechnology, a section of the journal Frontiers in Bioengineering and Biotechnology

RECEIVED 18 February 2023
ACCEPTED 14 March 2023
PUBLISHED 23 March 2023

CITATION
Shi X, Liu J and Wang G (2023), A peroxidase-like magneto-gold nanozyme AuNC@Fe_3O_4 with photothermal effect for induced cell apoptosis of hepatocellular carcinoma cells *in vitro*.
Front. Bioeng. Biotechnol. 11:1168750.
doi: 10.3389/fbioe.2023.1168750

A peroxidase-like magneto-gold nanozyme AuNC@Fe_3O_4 with photothermal effect for induced cell apoptosis of hepatocellular carcinoma cells *in vitro*

Xinglong Shi[1†], Jifa Liu[1,2†] and Guannan Wang[1*]

[1]College of Medical Engineering & the Key Laboratory for Medical Functional Nanomaterials, Jining Medical University, Jining, China, [2]Cheeloo College of Medicine, Shandong University, Jinan, China

Hepatocellular carcinoma (HCC) is one of the most commonly diagnosed and malignant cancers worldwide. Conventional therapy strategies may not completely eradicate the tumor and may cause side effects during treatment. Nano-catalytic therapy, as a novel strategy, has attracted a great deal of attention. This study aimed to synthesize a multifunctional magneto-gold nanozyme AuNC@Fe_3O_4 and evaluate its anti-cancer potential in HepG2 cells *in vitro*. The characteristics of AuNC@Fe_3O_4 were assessed using a transmission electron microscope, dynamic light scattering, and energy-dispersive X-ray. The photothermal performance and peroxidase (POD)-like activity of AuNC@Fe_3O_4 were detected, using thermal camera and ultraviolet-visible spectrophotometer, respectively. The anti-cancer potential of AuNC@Fe_3O_4 was examined using cell counting kit-8, live/dead cell staining, and apoptosis analysis. Further research on HepG2 cells included the detection of intracellular reactive oxygen species (ROS) and lysosomal impairment. We observed that the AuNC@Fe_3O_4 had a small size, good photothermal conversion efficiency and high POD-like activity, and also inhibited cell proliferation and enhanced cell apoptotic ability in HepG2 cells. Furthermore, the AuNC@Fe_3O_4 enhanced ROS production and lysosomal impairment *via* the synergistic effect of photothermal and nano-catalytic therapies, which induced cell death or apoptosis. Thus, the magneto-gold nanozyme AuNC@Fe_3O_4 may offer a potential anti-cancer strategy for HCC.

KEYWORDS

POD-like, magneto-gold, nanozyme, photothermal effect, cell apoptosis, hepatocellular carcinoma

1 Introduction

Data from Global Cancer Incidence, Mortality and Prevalence 2020 revealed that liver cancer was the sixth commonly diagnosed and the third lethal cancer worldwide (Sung et al., 2021). China accounted for 23.7% and 30% of the global morbidity and mortality from liver cancer, respectively (Ferlay et al., 2021). It was predicted that between 2020 and 2040, there would be a 55% increase in the number of new cases of liver cancer per year, and the percentage of people who would die from the disease in 2040 would be more than 56.4% of those in 2020 (Rumgay et al., 2022). Primary liver cancer can be classified into three types: cholangiocarcinoma, hepatocellular carcinoma (HCC), and a combination of the two, with HCC accounting for approximately 90% of all cases (Llovet et al., 2016). HCC progression is

influenced by several risk factors, such as alcohol abuse, smoking, toxic chemicals, and hepatitis virus (especially for HBV) infections (Yang et al., 2019). Owing to the absolute number of HBV-infected populations (Liu et al., 2016), the mortality rate of HBV-related liver cancer was consistently higher than the global level (Liu et al., 2019), which increased the burden of HCC in China.

In most cases, conventional treatments, such as surgery, radiation, and chemotherapy, do not completely eradicate the tumor and may cause side effects during treatment, such as cancer palindromia and drug resistance (Zhu et al., 2016; Xu et al., 2019; Raoul and Edeline, 2020; Liu and Song, 2021). For example, the surgery was initially considered to be used for patients with early-stage HCC; However, over 50% of patients experienced a recurrence within a year following surgery (Gil et al., 2015; Weber et al., 2015). Sorafenib was an option for patients with advanced-stage cancer, however, it was only effective in less than a third of them and caused drug tolerance or cytotoxicity (Llovet et al., 2008; Cheng et al., 2009; Bruix et al., 2012; Anwanwan et al., 2020). Besides surgery and chemotherapy, radiation therapy is a non-invasive and local ablative treatment approach to kill cancer cells. However, the efficiency of radiation therapy is easily limited by radioresistance, due to the DNA damage response and cell cycle checkpoints activation (Yoon and Seong, 2014; Wahl et al., 2016; Sun et al., 2020). Although the traditional strategies of HCC control the growth of HCC and prolong the survival time of patients, it still cannot satisfy their needs. Thus, it is necessary to discover a more efficient treatment approach to improve the quality of life for patients.

In recent years, nano-catalytic therapy, as a new tumor treatment strategy, has attracted the attention of an increasing number of researchers. Nanozymes are nanomaterials that catalyze chemical reactions of substrates under physiological states, obeying the patterns of enzyme kinetics (Wei et al., 2021). In 2007, Yan's team was the first to report that magnetic nanoparticles Fe_3O_4 possessed peroxidase (POD)-like activity, and proposed the concept of nano-catalysis (Gao et al., 2007). Furthermore, Shi *et al.* innovatively paved the way for further applications of nanoparticles in tumor nano-catalytic therapy, by disrupting the Fenton reaction that induced H_2O_2 disproportionation for •OH generation (Zhang et al., 2016). Currently, nano-catalytic therapy and photothermal therapy (PTT) are frequently employed in the treatment of tumors. The integration of PTT and nano-catalytic therapy has contributed to improving their cancer therapy efficiency. For instance, hyperthermia promoted the enzymatic activity of Fe_3O_4 nanozyme to generate more •OH, and simultaneously, •OH heightened the therapeutic impact of PTT (Wu et al., 2019; Zuo et al., 2022). It has also been reported that the Fe_3O_4@ZIF-8/GOx@MnO_2 hybrid nanozyme can enhance the efficiency of nanoparticles in anti-tumor therapy by combining multiple therapeutics (Zhang et al., 2021b).

Fe_3O_4 and Au nanoparticles, as is well known, demonstrated the unique characteristics of a high photothermal effect and POD-like activity (Zeng et al., 2013; Vallabani et al., 2017; Ghosh et al., 2022; Huang et al., 2022). Encouraged by the aforementioned description, we wonder if AuNC@Fe_3O_4 which has been employed as magnetic resonance imaging/com-puterized tomography multimodal imaging contrast agents of cancer owing to their high relaxivity value and excellent contrast enhancement (Wang et al., 2016b), also retains the photothermal and catalytic ability, or is beneficial to cancer therapy.

In this study, we synthesized multifunctional magneto-gold nanozyme AuNC@Fe_3O_4 and evaluated their anti-cancer ability in HCC cells *in vitro*. The AuNC@Fe_3O_4 exhibited high photothermal effect and POD-like activity. The results also reflected the influence of AuNC@Fe_3O_4 on engendering cell death and apoptosis. Furthermore, the synergistic effect of PTT and nano-catalytic therapy on reactive oxygen species (ROS) and lysosomal impairment in HepG2 cells were also studied.

2 Materials and methods

2.1 Materials and reagents

Ferric slat, gold (III) chloride (HAuCl4), other reagents related to AuNC@Fe_3O_4 synthesis and 3,3′,5,5′-Tetramethylbenzidine (TMB) were purchased from Sigma, Inc. (St. Louis, United States). H_2O_2 solution and different pH buffer solutions (pH = 2, 3, 4, 5, 6, 7, 8, and 9) were bought from Aladdin (Shanghai, China). Human umbilical vein endothelial cells (HUVEC), human HCC cell lines (HepG2 cells) and the specific culture mediums for the two cell lines were purchased from Procell (Wuhan, China). Cell Counting Kit-8 (CCK-8) was obtained from Sangon Biotech (Shanghai, China). 2′,7′-Dichlorodihydrofluorescein diacetate (DCFH-DA) was obtained from MedChemExpress (New Jersey, United States). Calcein-AM/propidium iodide (PI) kit, Annexin V-FITC apoptosis detection kit, Lyso-Tracker Red kit and Hoechst 33342 staining solution were purchased from Beyotime. Inc. (Shanghai, China).

2.2 AuNC@Fe_3O_4 synthesis

The AuNC@Fe_3O_4 was synthesized according to previous methods (Wang et al., 2016b). AuNC was initially synthesized and coated with poly (vinyl pyrrolidone) (PVP). Subsequently, PVP was replaced with 2-aminoethanethiol, and AuNC was transformed into AuNC-NH2 for interacting with carboxyl group functionalized Fe_3O_4 nanoparticles. The ultra-small Fe_3O_4 particles were prepared. To produce Fe_3O_4-COOH, ferric slats were vigorously stirred in pre-prepared polymer poly (acrylic acid) (PAA) solution. N-(3-Dimethylaminopropyl)-N-ethylcarbodiimide and N-hydroxysuccinimide activated the Fe_3O_4-COOH, which then reacted with AuNC-NH_2 to generate AuNC@Fe_3O_4. The AuNC@Fe_3O_4 was centrifugated, washed with ethanol and water, and then dispersed in ddH_2O with different concentrations for further experiments.

2.3 AuNC@Fe_3O_4 characterization

The size of AuNC or AuNC@Fe_3O_4 nanoparticles was analyzed using a transmission electron microscope (TEM). Dynamic light scattering (DLS) was applied to detect hydrodynamic particle diameter and intensity of AuNC@Fe_3O_4 nanoparticles on a Malvern Zetasizer NANO ZS. Energy-dispersive X-ray (EDX)

was utilized to analysis the element of AuNC@Fe_3O_4 nanoparticles on a FEI TECNAI G20 high-resolution TEM.

2.4 AuNC@Fe_3O_4 photothermal performance *in vitro*

To investigate the photothermal effect of the magneto-gold nanoparticles, First, 200 µl of AuNC@Fe_3O_4 solution with distinct concentrations (0, 50, 100, 200, 300, 400, and 500 µg/ml) was exposed to 808 nm laser at 1.0 W for 720 s; Second, 200 µl of AuNC@Fe_3O_4 solution with concentration of 50 µg/ml was exposed to 808 nm laser at different powers (1.0, 1.2, and 1.4 W) for 720 s. The thermal image and temperature change were recorded at different times by an infrared (IR) thermal camera (Fotric 220). As a control, ddH_2O was irradiated under the same conditions.

To investigate the photothermal stability of the magneto-gold nanoparticles, AuNC@Fe_3O_4 aqueous solution (500 µg/ml) was irradiated under 808 nm laser at 1.0 W for 420 s, then the irradiation was turned off. After that, the temperature was further measured for another 360 s. The experiment was then repeated four more times. The thermal image and temperature change were recorded at different times by the IR thermal camera (Fotric 220). As a control, ddH_2O was irradiated under the same operation.

To evaluate the photothermal conversion efficiency of AuNC@Fe_3O_4, the data from the cooling periods were calculated, according to previous report (Ren et al., 2015). Briefly, when the system reached energy balance, the equation was:

$$\sum_i m_i C_{p,i} \frac{dT}{dt} = Q_{AuNC@Fe_3O_4} + Q_s - Q_{loss} \tag{1}$$

where C*p* and m were the heat capacity and mass of AuNC@Fe_3O_4 solution, respectively. *T* was the temperature of AuNC@Fe_3O_4 solution. $Q_{AuNC@Fe_3O_4}$ represented energy absorbed by AuNC@Fe_3O_4 nanoparticles. Q_s represented the energy absorbed by ddH_2O. Q_{loss} was the heat lost to the surroundings.

The equation for $Q_{AuNC@Fe_3O_4}$ was:

$$Q_{AuNC@Fe_3O_4} = I\left(1 - 10^{-A_\lambda}\right)\eta \tag{2}$$

where *I* represented the laser power density, A_λ denoted the absorbance of AuNC@Fe_3O_4 solution under 808 nm in a 96-well plate, and η represented its photothermal conversion efficiency.

The equation for Q_{loss} was

$$Q_{loss} = hA\Delta T \tag{3}$$

where *A* was the surface area of the container, *h* denoted the heat transfer coefficient; ΔT represented the temperature changes, expressed as T-T_{surr} (where T and T_{surr} represent the solution and surrounding air temperature, respectively).

When heating ddH_2O, the heat input and output reached energy balance at the maximum steady-state temperature, therefore the equation for Q_s was:

$$Q_s = Q_{loss} = hA\Delta T_{max,H_2O} \tag{4}$$

where $\Delta T_{max,H_2O}$ was the temperature changes of ddH_2O.

When the system reached its maximum balanced temperature, the energy input (the heat absorbed by AuNC@Fe_3O_4 and ddH_2O) was equal to the heat lost into the surrounding, and the equation could be:

$$Q_{AuNC@Fe_3O_4} + Q_s = Q_{loss} = hA\Delta T_{max,mix} \tag{5}$$

where $\Delta T_{max,mix}$ was the changed temperature of the AuNC@Fe_3O_4 solution.

According to Eqs 2, 4, 5, η was:

$$\eta = \frac{hA\Delta T_{max,mix} - hA\Delta T_{max,H_2O}}{I\left(1 - 10^{-A_\lambda}\right)} = \frac{hA\left(\Delta T_{max,mix} - \Delta T_{max,H_2O}\right)}{I\left(1 - 10^{-A_\lambda}\right)} \tag{6}$$

To calculate the unknown *hA*, θ was introduced, and could be expressed as following:

$$\theta = \frac{\Delta T}{\Delta T_{max}} \tag{7}$$

Adding Eq. 7 into Eq. 1, the new equation could be:

$$\frac{d\theta}{dt} = \frac{hA}{\sum_i m_i C_{p,i}}\left(\frac{Q_{AuNC@Fe_3O_4} + Q_s}{hA\Delta T_{max}} - \theta\right) \tag{8}$$

During the cooling period, the $Q_{AuNC@Fe_3O_4} + Q_s = 0$ in Eq. 8 was:

$$dt = -\frac{\sum_i m_i C_{p,i}}{hA}\frac{d\theta}{\theta} \tag{9}$$

which could be changed as following:

$$t = -\frac{\sum_i m_i C_{p,i}}{hA} ln\,\theta \tag{10}$$

where $\frac{\sum_i m_i C_{p,i}}{hA}$ was calculated by time versus -ln(θ) plot. Since the mass of AuNC@Fe_3O_4 (1×10^{-7} kg) was relatively small when compared to that of ddH_2O ($m = 2 \times 10^{-4}$ kg), its m and Cp were neglected. The value of *hA* was then calculated using m_{H_2O} of 2×10^{-3} kg; C_{p,H_2O} of 4.2×10^3 J/(Kg.°C). Furthermore, the η of AuNC@Fe_3O_4 was determined by substituting the value of *hA* and other parameters into Eq. 6. The values of other parameters were as follows: $I = 2.3$ W/cm^2, $A_\lambda = 0.105$, $\Delta T_{max,mix} = 25.3$, and $\Delta T_{max,H_2O} = 0.1$.

2.5 POD-like activity assay

To evaluate the catalytic properties of AuNC@Fe_3O_4, AuNC@Fe_3O_4 (final concentration: 0, 5, 10, 20, 50, and 100 µg/ml), TMB (final concentration: 0.4 mM), and H_2O_2 (final concentration: 50 µM) was added into a final volume of 500 µl of phosphate-buffered saline (PBS) solution. The absorbance of the buffer was measured using an ultraviolet-visible (UV-vis) spectrophotometer at 500–800 nm. The POD-like activity assay of AuNC@Fe_3O_4 at varying pH levels (pH = 2, 3, 4, 5, 6, 7, 8, and 9) was performed in the presence of H_2O_2 and TMB in PBS solution, and the absorbance at 652 nm was detected by a microplate reader.

2.6 POD-like catalytic kinetic determination

When TMB was used as a substrate, the AuNC@Fe_3O_4 (final concentration: 50 µg/mL), TMB (final concentration: 0.0, 0.2, 0.4, 0.6, and 0.8 mM), and H_2O_2 (final concentration: 50 µM) was added into a final volume of 100 µl of PBS solution. The absorbance at 652 nm was detected by a microplate reader.

When H_2O_2 was used as a substrate, the AuNC@Fe_3O_4 (final concentration: 50 μg/ml), H_2O_2 (final concentration: 0, 10, 20, 30, 40, 50, 60, 70, and 80 μM) and TMB (final concentration: 0.4 mM) was added into a final volume of 100 μl of PBS solution. The absorbance at 652 nm was detected by a microplate reader.

Based on Michaelis-Menten Eq. 11 and saturation curve, the V_{max} and Michaelis-Menten constant could be calculated,

$$\frac{1}{V} = \frac{K_m}{V_{max}} \frac{1}{[s]} + \frac{1}{V_{max}} \tag{11}$$

and the V was calculated using Eq. 12:

$$V = \frac{A}{(b \times \varepsilon_{652\,nm} \times t)} \tag{12}$$

where A was the absorbance of the reaction system at 652 nm. t = 600 s, which was the reaction time. b = 0.3125 cm, which was the light path in the reaction solution, and $\varepsilon_{652\,nm}$ = 39,000 M^{-1} cm^{-1} (Dashtestani et al., 2019).

2.7 Cell viability assay

The HepG2 and the HUVEC cells were cultured to assess the cytotoxicity of AuNC@Fe_3O_4 through CCK-8 assay. 4000 of cells were cultured at 96-well plate well overnight at 37°C in a humidified incubator with 5% CO_2. Subsequently, 100 μl of fresh medium with distinct concentrations of AuNC@Fe_3O_4 (0, 10, 20, 30, 40, and 50 μg/ml) was changed and cultured for 24 h. The CCK-8 solution (final volume: 10 μl) was added into 100 μl of medium, and incubated for 2 h. Then, the absorbance of medium was detected at 450 nm.

2.8 Live/dead cell staining assay

HepG2 cells were cultured overnight in a 12-well plate with 500 μl of culture medium. The cells were then treated with PBS or AuNC@Fe_3O_4 (50 μg/ml) for 12 h. Then, the cells were cultured for an additional 12 h after either being irradiated by an 808 nm laser for 5 min at 1.4 W or not. The culture medium was then removed, and cells were washed once with PBS and incubated with 500 μl stain solution for 15 min. Finally, the cells were washed thrice with PBS and photographed by an inverted fluorescence microscope.

2.9 Apoptosis analysis

To investigate the ability of AuNC@Fe_3O_4 for inducing cell apoptosis, HepG2 cells were quantitatively detected by a flow cytometer. The cells were initially seeded into a 6-well plate and treated under different conditions for 24 h. They were collected with 0.25% trypsin and washed thrice with ice-cold PBS. Subsequently, these cells were resuspended in 195 μl of binding buffer. Ten microliters of PI and 5 μl of Annexin V-FITC were added, and the mixture was incubated for 20 min at room temperature, and cells were detected by flow cytometer.

2.10 Intracellular ROS detection

The intracellular POD-like catalytic ability of AuNC@Fe_3O_4 was detected using DCFH-DA. Except for an additional 4 h of culture, the method used for the laser-irradiated groups was similar to the treatment described above. Furthermore, 1 ml of PBS with DCFH-DA (5 μM) was added, and the mixture was incubated for another 30 min at 37°C in a humidified incubator with 5% CO_2. The wells were then washed thrice with PBS to remove the excess dye and photographed by an inverted fluorescence microscope.

2.11 Lysosomal impairment assay

After treatment, lysosomes and cell nuclei were stained with Lyso-Tracker Red and Hoechst 33342, respectively, according to the manufacturer's instructions. Subsequently, an inverted fluorescence microscope was used to capture images of cells.

2.12 Statistical analysis

Statistical analysis was achieved by GraphPad Prism version 8 (GraphPad Software, United States). Results were represented as mean ± standard deviation. The student t-test was used to compare the means of multiple groups. The statistical significances were as follows: * $0.01 < p < 0.05$, ** $0.001 < p < 0.01$, and ***$p < 0.001$.

3 Results and discussion

3.1 Synthesis and characterization of AuNC@Fe_3O_4

The structure and characteristics of AuNC and AuNC@Fe_3O_4 were determined by TEM. The results demonstrated that the diameter of AuNC and AuNC@Fe_3O_4 were 25–40 and 50–100 nm, respectively, with high uniformity and no agglomeration (Figures 1A, B). DLS was used to confirm the size of AuNC@Fe_3O_4, and the average hydrodynamic size distribution of these nanoparticles was approximately 55 nm (Figure 1C). The increase in the hydrodynamic size might be owing to the attachment of Fe_3O_4 to the surface of the AuNC. Elemental mapping analysis revealed the presence of the atoms Au, Fe and O, proving that AuNC@Fe_3O_4 was successfully formed (Figure 1D; Table 1). The "-CO-NH-", that came from the reaction of Fe_3O_4-COOH and AuNC-NH_2 and the carbon-coated brace used during sample preparation or analysis might have contributed to the existence of C element that was also present (Phongtongpasuk et al., 2016).

3.2 Photothermal performance of AuNC@Fe_3O_4

The thermal camera was used to investigate the photothermal conversion capabilities of AuNC@Fe_3O_4. The temperature changes of AuNC@Fe_3O_4 solution with different concentrations under

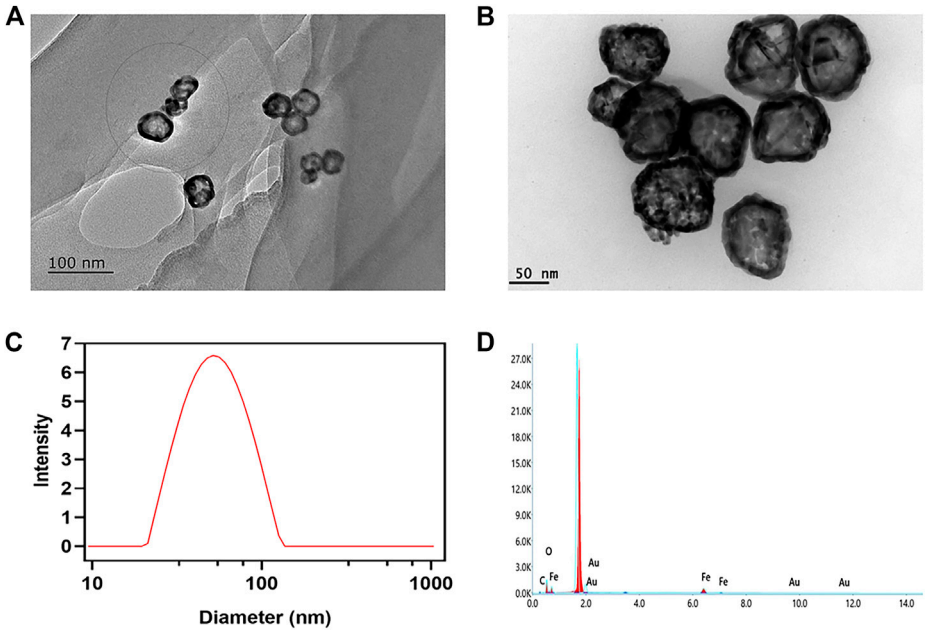

FIGURE 1
Characterization of AuNC@Fe_3O_4. **(A)** Transmission electron microscope (TEM) images of AuNC. Scale bar: 100 nm. **(B)** TEM images of AuNC@Fe_3O_4. Scale bar: 50 nm. **(C)** Dynamic light scattering (DLS) result of AuNC@Fe_3O_4. **(D)** Energy-dispersive X-ray (EDX) result of AuNC@Fe_3O_4.

TABLE 1 The statistics of elements analysis for AuNC@Fe_3O_4 by energy-dispersive X-ray (EDX).

Compound	Element	Weight (%)
AuNC@Fe_3O_4	Au	23.1
	Fe	29.4
	O	42.4
	C	5.1

808 nm laser irradiation at 1.0 W for 360 s were recorded. As depicted in Figure 2A, the temperature of the solution increased in a concentration- and time-dependent pattern. For example, the temperature of different concentrations of AuNC@Fe_3O_4 solution reached steady statue at 8 min. The temperature of AuNC@Fe_3O_4 solution (500 μg/ml) was changed significantly from 25.9°C to 52.3°C compared with the neglected increase in that of ddH_2O (from 26.0°C to 26.5°C), indicating the good photothermal response of AuNC@Fe_3O_4. For further investigation, the AuNC@Fe_3O_4 solution (50 μg/ml) was irradiation at different powers (1.0, 1.2, and 1.4 W). The laser power was increased from 1.0 to 1.4 W, which resulted in a significant increase in the temperature of the AuNC@Fe_3O_4 solution. A temperature of 45.3°C was achieved after 10 min of 808 nm laser irradiation at 1.4 W (Figure 2B). PTT, a promising cancer treatment strategy, converts light energy into heat to generate an area of hyperthermia, where tissues can be exposed to high temperatures (from 42°C to 45°C), which can damage or kill tumor cells (Tchouagué et al., 2019; Qu et al., 2022). The results of Figures 2A, B suggested a potential application of AuNC@Fe_3O_4 in anti-tumor.

Additionally, five cycles of the "On and Off" model were used to measure the temperature curve of the AuNC@Fe_3O_4 solution to assess its photothermal stability. The AuNC@Fe_3O_4 showed excellent photothermal stability since the temperature was raised to 52.9 °C and there was no reduction in the temperature rise following laser irradiation during the five cycles (Figure 2D).

Moreover, the average of the data from the five cooling periods was used to get the photothermal conversion efficiency (η) of AuNC@Fe_3O_4. The plot of the time value and −ln (θ) was displayed in Figure 2E, and its slope was 99.526. Using Eqs 6, 10, the η of AuNC@Fe_3O_4 was calculated to be 39.58%, which was similar with or higher than the PPT reagents previously reported, such as, EA-Fe@BSA NPs (31.2%) (Tian et al., 2020), Fe_3O_4@Carbon@Platinum-Chlorin e6 (28.28%) (Xu et al., 2022b), Au nanorods (22%) (Zeng et al., 2013), Au nanoshells (13%) (Hessel et al., 2011), PANi@Au (40.4%) and Au nanoparticles (21.7%) (Zhang et al., 2021a).

Collectively, these findings suggested that AuNC@Fe_3O_4 exhibited good photothermal conversion and photothermal stability, which implied a promising application in PTT for tumors.

3.3 POD-like activity of AuNC@Fe_3O_4

It was reported that Au and Fe_3O_4 nanoparticles demonstrated POD-like enzyme activity (Zandieh and Liu, 2021), therefore it was necessary to investigate whether the AuNC@Fe_3O_4 possessed similar characteristics. The peroxidase mimicking activity of AuNC@Fe_3O_4 was validated by TMB. TMB could be oxidized to blue oxTMB by •OH and detected at 652 nm, using UV-vis spectrophotometer (Zhu et al., 2022). As presented in Figure 3A,

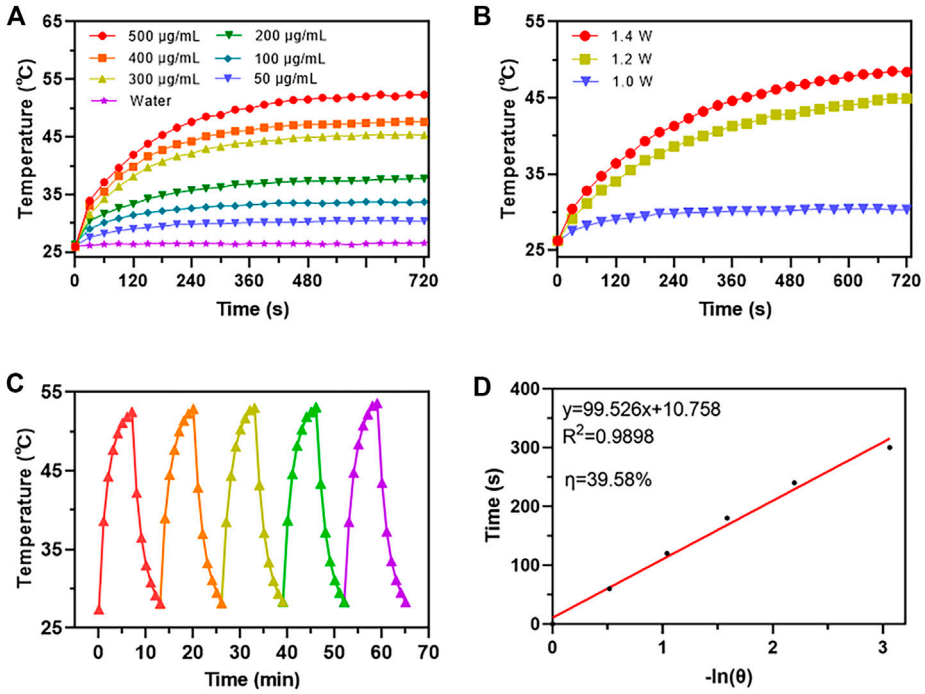

FIGURE 2
Photothermal performance analysis of AuNC@Fe_3O_4. **(A)** Temperature change curves of water and AuNC@Fe_3O_4 aqueous solution after different treatments **(B)** Temperature change curves of AuNC@Fe_3O_4 after different treatments **(C)** Photostability of AuNC@Fe_3O_4 solution under irradiation for five cycles. **(D)** Time versus -ln(θ) plot of the AuNC@Fe_3O_4 solution.

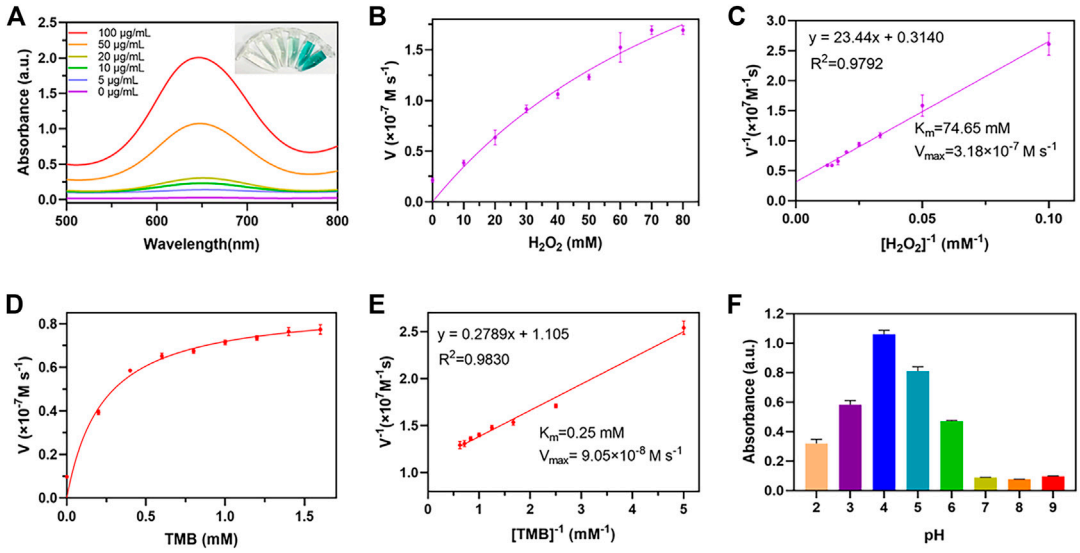

FIGURE 3
POD-like activity assay of AuNC@Fe_3O_4. **(A)** Ultraviolet-visible (UV-vis) absorption spectra of the reaction system with different concentrations. **(B)** Michaelis-Menten curve of AuNC@Fe_3O_4 for H_2O_2. **(C)** Lineweaver-Burk plotting of AuNC@Fe_3O_4 for H_2O_2. **(D)** Michaelis-Menten curve of AuNC@Fe_3O_4 for TMB. **(E)** Lineweaver-Burk plotting of AuNC@Fe_3O_4 for TMB. **(F)** The absorbance of the reaction system at 652 nm under different pH values.

the groups with different concentrations of AuNC@Fe_3O_4 had varying absorbance intensities at 652 nm. The group of AuNC@Fe_3O_4 with 100 μg/ml showed the strongest signal at 652 nm, followed by the group with 50 μg/ml. The intensity of absorbance tested with H_2O displayed no peak at 652 nm. These findings, which indicated that the AuNC@Fe_3O_4 possessed POD-like enzyme

activity, were further verified by the inset digital photos (Figure 3A). To further confirm the POD-like enzyme specificity of AuNC@Fe_3O_4, the UV-vis absorption spectra of the reaction system with varying conditions was collected. It was observed from Supplementary Figure S1 that absorbance peak of the AuNC@Fe_3O_4+TMB or AuNC@Fe_3O_4+H_2O_2 group was negligible. In the absence of AuNC@Fe_3O_4, the TMB + H_2O_2, TMB or H_2O_2 group showed no significant absorbance peak at 652 nm, which was consistent with the AuNC@Fe_3O_4 only group. The results suggested that, except AuNC@Fe_3O_4, other components in the reaction system could hardly catalyzed the conversion of H_2O_2 to •OH and oxidized TMB, which indicated AuNC@Fe_3O_4 exhibited a specific activity of POD-like enzyme.

Kinetic parameters were analyzed to quantitate the POD-like activity of AuNC@Fe_3O_4 using the initial rate method (Gao et al., 2017). First, the absorbance of the system was measured, while varying the concentrations of H_2O_2 concentrations from 0 to 80 mM and maintaining a TMB concentration of 0.4 mM (Supplementary Figure S2). Second, the velocity of reaction was calculated according Eq. 12 and the plot was consistent with traditional Michaelis-Menten curve (Figure 3B), which demonstrates that the catalytic reaction rate increased with the growth of substrate concentration and achieved steady state at high concentrations (Huang et al., 2022). Third, after Lineweaver-Burk fitting, the enzyme kinetic parameters, such as Michaelis-Menten constants (K_m) was calculated to be 47.65 mM and the maximum reaction velocity (V_{max}) was 3.18×10^{-7} M s^{-1} (Figure 3C). Forth, the absorbance of the solution was measured at 652 nm while varying TMB concentrations and maintaining H_2O_2 concentration as a constant (Supplementary Figure S3). Last, the K_m and V_{max} were 0.25 mM and 9.03×10^{-8} M s^{-1} respectively, and the results were presented in Figures 3D, E.

When the H_2O_2 was used as substrate, the velocity of AuNC@Fe_3O_4 was faster than that of Fe_3O_4 (Vallabani et al., 2017), and K_m value that was lower than that of Fe_3O_4 (Vallabani et al., 2017). Similarly, when the TMB was used as substrate, AuNC@Fe_3O_4 had a velocity that was faster than that of Au NRT, Au NC, Au NS, and horseradish peroxidase (Ghosh et al., 2022), and its value of K_m was also lower than those of them. In the catalytic reaction system, the K_m represents the affinity between the enzyme and substrates, and the lower the K_m, the higher enzyme affinity (Jiang et al., 2018). Therefore, the results suggested that the catalytic ability and the affinity between AuNC@Fe_3O_4 nanozyme and substrates (such as TMB and H_2O_2) was stronger than that of Fe_3O_4 and Au nanoparticles. The following factors may contribute to the significant increase in POD-like activity of AuNC@Fe_3O_4 nanoparticles: the electronic structure of the interfaces between the Fe_3O_4 and Au, the synergistic effect, and polarization effects from Au to Fe_3O_4 (Lee et al., 2010; Sun et al., 2013; Wang et al., 2016a).

Considering the complex tumor microenvironment, such as hypoxia and weak acidity (Li et al., 2020; Zhao et al., 2021), it was unclear whether AuNC@Fe_3O_4 exhibits POD-like enzyme activity even at low pH. At low pH values ranging from 2 to 6, the AuNC@Fe_3O_4 exhibited higher POD-like enzyme activity, and the optional pH was 4. When the pH was higher than 7, the POD-like enzyme activity was reduced dramatically (Figure 3F). The results hinted that AuNC@Fe_3O_4 might have significantly varied POD-like enzyme activity between distinct parts of normal (pH = 7.4) and cancer tissues (pH = 6.5), especially for lysosomes (pH = 4.5–5.5) and endosomes (pH = 5.5–6.8) (Kuppusamy et al., 2002; Wojtkowiak et al., 2011).

Overall, these findings provided evidence for the high POD-like catalytic activity of AuNC@Fe_3O_4 nanozyme and implied potential catalytic ability in tumor.

3.4 *In vitro* anti-tumor effect of AuNC@Fe_3O_4

It is important to examine the biocompatibility of AuNC@Fe_3O_4 before performing further clinical applications. Therefore, HepG2 and HUVEC cells were incubated with AuNC@Fe_3O_4 at varying concentrations for 24 h to estimate the cytotoxicity using CCK-8 assay. Low concentrations of AuNC@Fe_3O_4 did not affect the survival rate of HepG2 cells; however, at 40 and 50 μg/ml, the viability of cells decreased to 77% and 60%, respectively (Figure 4A). In contrast, the viability of HUVEC cells was not drastically affected by AuNC@Fe_3O_4 after 24 h incubation at the varying treatments (Figure 4B). The findings indicated that AuNC@Fe_3O_4 was not toxic to normal cells at the concentration ranging from 0 μg/ml to 50 μg/ml and demonstrated good biocompatibility. The reason why AuNC@Fe_3O_4 showed more sensitive to HepG2 could be attributed to the fact that the pH of the tumor was lower than that of normal tissues (Kuppusamy et al., 2002; Wojtkowiak et al., 2011) and that the AuNC@Fe_3O_4 had higher POD-like enzyme activity in a lower pH reaction system, which meant it produced more •OH, which could be lethal to cells (Cui et al., 2018; Malfanti et al., 2022).

To explore the anti-tumor effect of AuNC@Fe_3O_4, the live/dead cell staining assay was utilized. There were nearly no dead cells in the PBS and PBS + NIR (near-infrared) groups; However, when the cells were treated with AuNC@Fe_3O_4 or AuNC@Fe_3O_4+NIR, the number of dead cells increased significantly, with the last group having the most cell death (Figure 4C). To further verify this result, the flow apoptosis assays of HepG2 cells with different conditions was conducted. As depicted in Figures 4D, E; Supplementary Table S1, the results indicated that approximately 51% apoptotic cells (Q2+Q3) were observed in the AuNC@Fe_3O_4+NIR group, which was greater than other groups.

The results revealed that AuNC@Fe_3O_4 displayed good biocompatibility, and the laser irradiation augmented the anti-tumor ability of AuNC@Fe_3O_4.

3.5 ROS and lysosomal impairment induced by AuNC@Fe_3O_4

To confirm the synergistic effect of PTT and POD-like enzyme catalytic activity of AuNC@Fe_3O_4, the production of the ROS in HepG2 cells was validated using the DCFH-DA probe. As reported, DCFH-DA crossed the cell membrane and was subsequently oxidized to DCF with green fluorescence (Afri et al., 2004). It was evident from Figure 5A that the HepG2 cells incubated with AuNC@Fe_3O_4 exhibited a higher green fluorescence signal than PBS and PBS + NIR, indicating the ability of AuNC@Fe_3O_4 to effectively

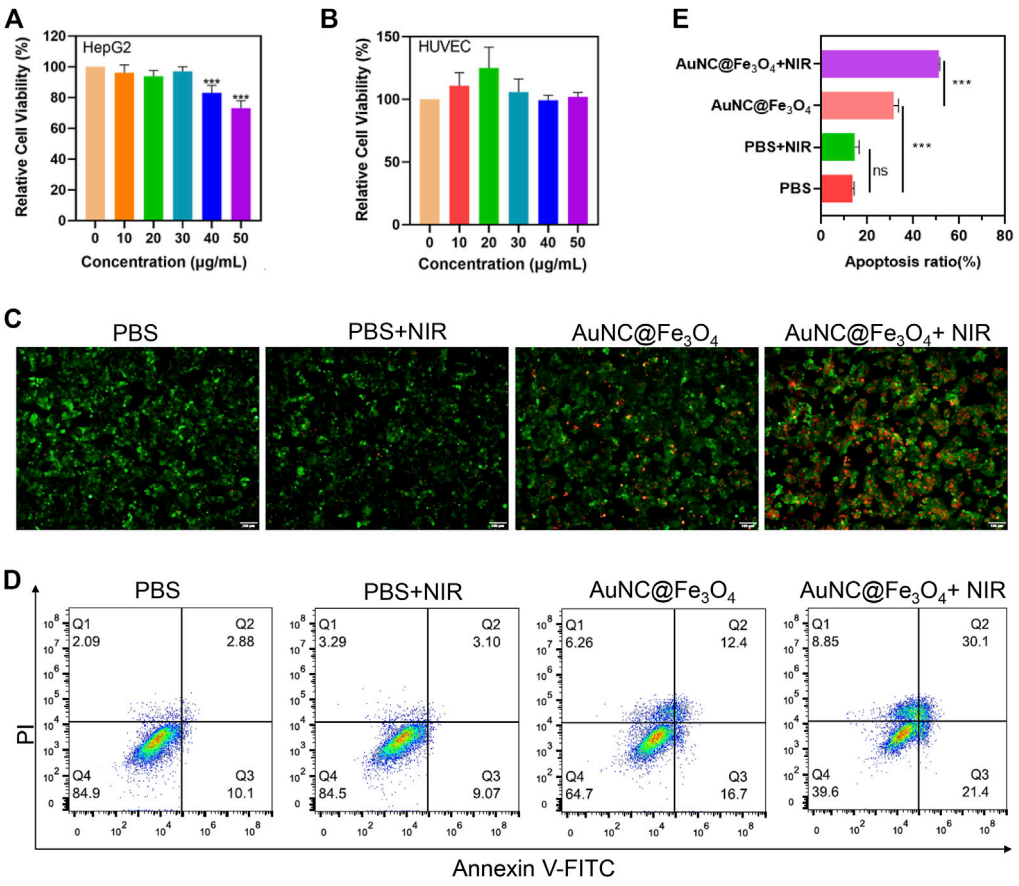

FIGURE 4
Evaluation for anti-tumor effect of AuNC@Fe_3O_4 *in vitro*. **(A)** Cell viability of HepG2 cells treated with AuNC@Fe_3O_4 for 24 h. **(B)** Cell viability of human umbilical vein endothelial cells (HUVEC) cells treated with AuNC@Fe_3O_4 for 24 h. **(C)** Calcein-Am/propidium iodide (PI) staining of HepG2 cells under different conditions. Scale bar: 100 μm. **(D)** Apoptosis analysis of HepG2 cells with different treatments. **(E)** The histogram results of apoptotic HepG2 cells derived from **(D)**. * $0.01 < p < 0.05$, ** $0.001 < p < 0.01$, and *** $p < 0.001$.

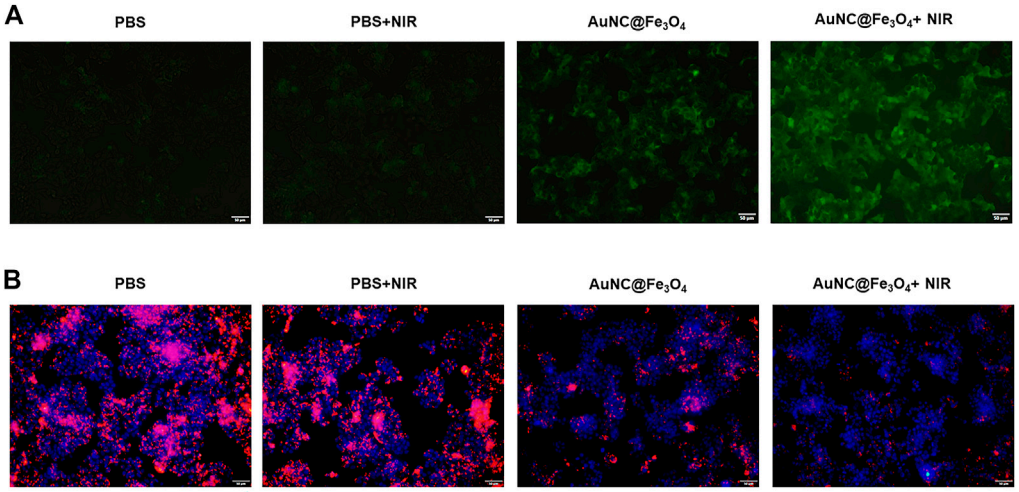

FIGURE 5
Analysis for synergistic effect of photothermal therapy (PTT) and catalytic activity of AuNC@Fe_3O_4. **(A)** Reactive oxygen species (ROS) detection of HepG2 cells with varying treatments. **(B)** Lysosomal impairment detection of HepG2 cells with varying treatments. Scale bar: 50 μm.

catalyze the conversion of intracellular H_2O_2 into •OH in cancer cells. Compared with the AuNC@Fe_3O_4 group, the signal of the AuNC@Fe_3O_4+NIR group was stronger. The similar result was collected by the detection of the absorbance intensities at 652 nm of the reaction system with or without NIR irradiation, using UV-vis spectrophotometer. We found the signal of reaction system with NIR irradiation was higher than that of group without irradiation (Supplementary Figure S4). The results confirmed that photothermal effect enhanced the POD-like enzyme catalytic activity of AuNC@Fe_3O_4.

The phenomenon could be attributed to the localized surface plasmon resonance (LSPR), which was the collective oscillation of surface free electrons in metal nanoparticles under light irradiation, leading to local heating (also called photothermal effect) and hot carriers (such as hot electrons and hot holes). One hand, energy of hot electrons may transfer to local heating by electron-phonon interactions, causing a rise in temperature (Brongersma et al., 2015). Similar with natural enzymes, the catalytic ability of nanozymes could be enhanced by elevated temperature (Wang et al., 2021; Zhu et al., 2022). Another hand, hot electrons could be transferred from AuNPs to empty orbits of H_2O_2, and activated the H_2O_2 to generate •OH under NIR light irradiation (Wang et al., 2017; Xu et al., 2022a).

It was reported that increased ROS could disrupt normal structure of the lysosomes (Shyam et al., 2021); however, whether the AuNC@Fe_3O_4 could induce lysosomal impairment remained unknown. The fluorescence images (Figure 5B) demonstrate that the PBS alone and PBS + NIR groups had negligible effects on the lysosomal impairment and that there were more HepG2 cells with lysosomal impairment following incubation with AuNC@Fe_3O_4. As expected, the lysosomal signal was the weakest in the AuNC@Fe_3O_4 under laser irradiation group. The results confirmed the synergistic effect of PTT and POD-like enzyme catalytic activity of AuNC@Fe_3O_4 on lysosomal impairment. Additionally, lysosomal impairment may contribute to an increase in lysosomal membrane permeability, a decrease in lysosomal quantity, a disruption in lysosomal enzyme activities, an increase in ROS levels, and most importantly, the induction of cell apoptosis (Abulikemu et al., 2022).

This at least partly, explained why AuNC@Fe_3O_4 with or without laser irradiation could cause cell death or apoptosis.

4 Conclusion

In summary, this study aimed to synthesize magneto-gold nanozyme AuNC@Fe_3O_4 and evaluate its anti-cancer effects for HCC *in vitro*. The AuNC@Fe_3O_4 showed the typical small size of about 55 nm. Additionally, it demonstrated a high photothermal conversion efficiency and POD-like activity. The CCK-8 results demonstrated that AuNC@Fe_3O_4 had good biocompatibility and HCC cell-killing ability. Moreover, AuNC@Fe_3O_4 could synergistically stimulate cell death or apoptosis. Finally, it was observed that magneto-gold nanocomposites could facilitate 808 nm laser irradiation to increase their catalytic ability to produce ROS. This might promote lysosomal impairment, causing cell death or apoptosis. These results suggested that the AuNC@Fe_3O_4 may offer a promising anti-cancer strategy for HCC *via* the synergistic effect of PTT and nano-catalytic therapy. Further research is required to investigate the therapeutic efficacy of AuNC@Fe_3O_4 for HCC *in vivo*.

Data availability statement

The original contributions presented in the study are included in the article/Supplementary Material, further inquiries can be directed to the corresponding author.

Author contributions

XS and GW proposed the conception and design of the study. XS and JL performed the experiments and interpretation of the data. XS and JL drafted the manuscript. GW reviewed and revised the manuscript. All authors read and approve the final manuscript.

Funding

This research was funded by Scientific Research Foundation of Jining Medical University (No.600768001) and Research Fund for Academician Lin He New Medicine (JYHL2022MS14).

Acknowledgments

We gratefully acknowledge support from Yangcui Qu, Haitao Han, Xueyan Wu and Huapeng Liu for technical support or donations in kind (e.g., equipments and reagents used for experiments).

Conflict of interest

The authors declare that the research was conducted in the absence of any commercial or financial relationships that could be construed as a potential conflict of interest.

Publisher's note

Supplementary material

The Supplementary Material for this article can be found online at: https://www.frontiersin.org/articles/10.3389/fbioe.2023.1168750/full#supplementary-material

References

Abulikemu, A., Zhao, X., Qi, Y., Liu, Y., Wang, J., Zhou, W., et al. (2022). Lysosomal impairment-mediated autophagy dysfunction responsible for the vascular endothelial apoptosis caused by silica nanoparticle via ROS/PARP1/AIF signaling pathway. *Environ. Pollut.* 304, 119202. doi:10.1016/j.envpol.2022.119202

Afri, M., Frimer, A. A., and Cohen, Y. (2004). Active oxygen chemistry within the liposomal bilayer. Part IV: Locating 2',7'-dichlorofluorescein (DCF), 2',7'-dichlorodihydrofluorescein (DCFH) and 2',7'-dichlorodihydrofluorescein diacetate (DCFH-DA) in the lipid bilayer. *Chem. Phys. Lipids* 131, 123–133. doi:10.1016/j.chemphyslip.2004.04.006

Anwanwan, D., Singh, S. K., Singh, S., Saikam, V., and Singh, R. (2020). Challenges in liver cancer and possible treatment approaches. *Biochim. Biophys. Acta Rev. Cancer* 1873, 188314. doi:10.1016/j.bbcan.2019.188314

Brongersma, M. L., Halas, N. J., and Nordlander, P. (2015). Plasmon-induced hot carrier science and technology. *Nat. Nanotechnol.* 10, 25–34. doi:10.1038/nnano.2014.311

Bruix, J., Raoul, J. L., Sherman, M., Mazzaferro, V., Bolondi, L., Craxi, A., et al. (2012). Efficacy and safety of sorafenib in patients with advanced hepatocellular carcinoma: Subanalyses of a phase III trial. *J. Hepatol.* 57, 821–829. doi:10.1016/j.jhep.2012.06.014

Cheng, A. L., Kang, Y. K., Chen, Z., Tsao, C. J., Qin, S., Kim, J. S., et al. (2009). Efficacy and safety of sorafenib in patients in the asia-pacific region with advanced hepatocellular carcinoma: A phase III randomised, double-blind, placebo-controlled trial. *Lancet Oncol.* 10, 25–34. doi:10.1016/s1470-2045(08)70285-7

Cui, Q., Wang, J. Q., Assaraf, Y. G., Ren, L., Gupta, P., Wei, L., et al. (2018). Modulating ROS to overcome multidrug resistance in cancer. *Drug Resist Updat* 41, 1–25. doi:10.1016/j.drup.2018.11.001

Dashtestani, F., Ghourchian, H., and Najafi, A. (2019). Silver-gold-apoferritin nanozyme for suppressing oxidative stress during cryopreservation. *Mater Sci. Eng. C Mater Biol. Appl.* 94, 831–840. doi:10.1016/j.msec.2018.10.008

Ferlay, J., Colombet, M., Soerjomataram, I., Parkin, D. M., PiñEROS, M., Znaor, A., et al. (2021). Cancer statistics for the year 2020: An overview. *Int. J. Cancer* 149, 778–789. doi:10.1002/ijc.33588

Gao, L., Zhuang, J., Nie, L., Zhang, J., Zhang, Y., Gu, N., et al. (2007). Intrinsic peroxidase-like activity of ferromagnetic nanoparticles. *Nat. Nanotechnol.* 2, 577–583. doi:10.1038/nnano.2007.260

Gao, L., Fan, K., and Yan, X. (2017). Iron oxide nanozyme: A multifunctional enzyme mimetic for biomedical applications. *Theranostics* 7, 3207–3227. doi:10.7150/thno.19738

Ghosh, S., Singh, P., Roy, S., Bhardwaj, K., and Jaiswal, A. (2022). Superior peroxidase-like activity of gold nanorattles in ultrasensitive H(2) O(2) sensing and antioxidant screening. *Chembiochem* 23, e202100691. doi:10.1002/cbic.202100691

Gil, E., Joh, J. W., Park, H. C., Yu, J. I., Jung, S. H., and Kim, J. M. (2015). Predictors and patterns of recurrence after curative liver resection in intrahepatic cholangiocarcinoma, for application of postoperative radiotherapy: A retrospective study. *World J. Surg. Oncol.* 13, 227. doi:10.1186/s12957-015-0637-z

Hessel, C. M., Pattani, V. P., Rasch, M., Panthani, M. G., Koo, B., Tunnell, J. W., et al. (2011). Copper selenide nanocrystals for photothermal therapy. *Nano Lett.* 11, 2560–2566. doi:10.1021/nl201400z

Huang, Y., Gu, Y., Liu, X., Deng, T., Dai, S., Qu, J., et al. (2022). Reusable ring-like Fe3O4/Au nanozymes with enhanced peroxidase-like activities for colorimetric-SERS dual-mode sensing of biomolecules in human blood. *Biosens. Bioelectron.* 209, 114253. doi:10.1016/j.bios.2022.114253

Jiang, B., Duan, D., Gao, L., Zhou, M., Fan, K., Tang, Y., et al. (2018). Standardized assays for determining the catalytic activity and kinetics of peroxidase-like nanozymes. *Nat. Protoc.* 13, 1506–1520. doi:10.1038/s41596-018-0001-1

Kuppusamy, P., Li, H., Ilangovan, G., Cardounel, A. J., Zweier, J. L., Yamada, K., et al. (2002). Noninvasive imaging of tumor redox status and its modification by tissue glutathione levels. *Cancer Res.* 62, 307–312.

Lee, Y., Garcia, M. A., Frey Huls, N. A., and Sun, S. (2010). Synthetic tuning of the catalytic properties of Au-Fe3O4 nanoparticles. *Angew. Chem. Int. Ed. Engl.* 49, 1271–1274. doi:10.1002/anie.200906130

Li, Y., Zhao, P., Gong, T., Wang, H., Jiang, X., Cheng, H., et al. (2020). Redox dyshomeostasis strategy for hypoxic tumor therapy based on DNAzyme-loaded electrophilic ZIFs. *Angew. Chem. Int. Ed. Engl.* 59, 22537–22543. doi:10.1002/anie.202003653

Liu, D., and Song, T. (2021). Changes in and challenges regarding the surgical treatment of hepatocellular carcinoma in China. *Biosci. Trends* 15, 142–147. doi:10.5582/bst.2021.01083

Liu, J., Zhang, S., Wang, Q., Shen, H., Zhang, M., Zhang, Y., et al. (2016). Seroepidemiology of Hepatitis B virus infection in 2 million men aged 21-49 years in rural China: A population-based, cross-sectional study. *Lancet Infect. Dis.* 16, 80–86. doi:10.1016/s1473-3099(15)00218-2

Liu, J., Liang, W., Jing, W., and Liu, M. (2019). Countdown to 2030: Eliminating Hepatitis B disease, China. *Bull. World Health Organ* 97, 230–238. doi:10.2471/blt.18.219469

Llovet, J. M., Ricci, S., Mazzaferro, V., Hilgard, P., Gane, E., Blanc, J. F., et al. (2008). Sorafenib in advanced hepatocellular carcinoma. *N. Engl. J. Med.* 359, 378–390. doi:10.1056/nejmoa0708857

Llovet, J. M., Zucman-Rossi, J., Pikarsky, E., Sangro, B., Schwartz, M., Sherman, M., et al. (2016). Hepatocellular carcinoma. *Nat. Rev. Dis. Prim.* 2, 16018. doi:10.1038/nrdp.2016.18

Malfanti, A., Catania, G., Degros, Q., Wang, M., Bausart, M., and Preat, V. (2022). Design of bio-responsive hyaluronic acid-doxorubicin conjugates for the local treatment of glioblastoma. *Pharmaceutics* 14, 124. doi:10.3390/pharmaceutics14010124

Phongtongpasuk, S., Poadang, S., and Yongvanich, N. (2016). Environmental-friendly method for synthesis of silver nanoparticles from dragon fruit peel extract and their antibacterial activities. *Energy Procedia* 89, 239–247. doi:10.1016/j.egypro.2016.05.031

Qu, Y., Lu, K., Zheng, Y., Huang, C., Wang, G., Zhang, Y., et al. (2022). Photothermal scaffolds/surfaces for regulation of cell behaviors. *Bioact. Mater* 8, 449–477. doi:10.1016/j.bioactmat.2021.05.052

Raoul, J. L., and Edeline, J. (2020). Systemic treatment of hepatocellular carcinoma: Standard of care in China and elsewhere. *Lancet Oncol.* 21, 479–481. doi:10.1016/s1470-2045(20)30082-6

Ren, W., Yan, Y., Zeng, L., Shi, Z., Gong, A., Schaaf, P., et al. (2015). A near infrared light triggered hydrogenated black TiO2 for cancer photothermal therapy. *Adv. Healthc. Mater* 4, 1526–1536. doi:10.1002/adhm.201500273

Rumgay, H., Arnold, M., Ferlay, J., Lesi, O., Cabasag, C. J., Vignat, J., et al. (2022). Global burden of primary liver cancer in 2020 and predictions to 2040. *J. Hepatol.* 77, 1598–1606. doi:10.1016/j.jhep.2022.08.021

Shyam, R., Ogando, D. G., Choi, M., Liton, P. B., and Bonanno, J. A. (2021). Mitochondrial ROS induced lysosomal dysfunction and autophagy impairment in an animal model of congenital hereditary endothelial dystrophy. *Invest. Ophthalmol. Vis. Sci.* 62, 15. doi:10.1167/iovs.62.12.15

Sun, H., Jiao, X., Han, Y., Jiang, Z., and Chen, D. (2013). Synthesis of Fe_3O_4-Au nanocomposites with enhanced peroxidase-like activity. *Eur. Chem. Soc. Publ.* 2013, 109. doi:10.1002/ejic.201201159

Sun, J., Zhu, Z., Li, W., Shen, M., Cao, C., Sun, Q., et al. (2020). UBE2T-regulated H2AX monoubiquitination induces hepatocellular carcinoma radioresistance by facilitating CHK1 activation. *J. Exp. Clin. Cancer Res.* 39, 222. doi:10.1186/s13046-020-01734-4

Sung, H., Ferlay, J., Siegel, R. L., Laversanne, M., Soerjomataram, I., Jemal, A., et al. (2021). Global cancer statistics 2020: GLOBOCAN estimates of incidence and mortality worldwide for 36 cancers in 185 countries. *CA Cancer J. Clin.* 71, 209–249. doi:10.3322/caac.21660

Tchouagué, M., Grondin, M., Glory, A., and Averill-Bates, D. (2019). Heat shock induces the cellular antioxidant defenses peroxiredoxin, glutathione and glucose 6-phosphate dehydrogenase through Nrf2. *Chem. Biol. Interact.* 310, 108717. doi:10.1016/j.cbi.2019.06.030

Tian, Q., An, L., Tian, Q., Lin, J., and Yang, S. (2020). Ellagic acid-Fe@BSA nanoparticles for endogenous H(2)S accelerated Fe(III)/Fe(II) conversion and photothermal synergistically enhanced chemodynamic therapy. *Theranostics* 10, 4101–4115. doi:10.7150/thno.41882

Vallabani, N. V. S., Karakoti, A. S., and Singh, S. (2017). ATP-mediated intrinsic peroxidase-like activity of Fe(3)O(4)-based nanozyme: One step detection of blood glucose at physiological pH. *Colloids Surf. B Biointerfaces* 153, 52–60. doi:10.1016/j.colsurfb.2017.02.004

Wahl, D. R., Stenmark, M. H., Tao, Y., Pollom, E. L., Caoili, E. M., Lawrence, T. S., et al. (2016). Outcomes after stereotactic body radiotherapy or radiofrequency ablation for hepatocellular carcinoma. *J. Clin. Oncol.* 34, 452–459. doi:10.1200/jco.2015.61.4925

Wang, C., Qian, J., Wang, K., Yang, X., Liu, Q., Hao, N., et al. (2016a). Colorimetric aptasensing of ochratoxin A using Au@Fe3O4 nanoparticles as signal indicator and magnetic separator. *Biosens. Bioelectron.* 77, 1183–1191. doi:10.1016/j.bios.2015.11.004

Wang, G., Gao, W., Zhang, X., and Mei, X. (2016b). Au nanocage functionalized with ultra-small Fe3O4 nanoparticles for targeting T1-T2Dual MRI and CT imaging of tumor. *Sci. Rep.* 6, 28258. doi:10.1038/srep28258

Wang, C., Shi, Y., Dan, Y. Y., Nie, X. G., Li, J., and Xia, X. H. (2017). Enhanced peroxidase-like performance of gold nanoparticles by hot electrons. *Chemistry* 23, 6717–6723. doi:10.1002/chem.201605380

Wang, X., Shi, Q., Zha, Z., Zhu, D., Zheng, L., Shi, L., et al. (2021). Copper single-atom catalysts with photothermal performance and enhanced nanozyme activity for bacteria-infected wound therapy. *Bioact. Mater* 6, 4389–4401. doi:10.1016/j.bioactmat.2021.04.024

Weber, S. M., Ribero, D., O'Reilly, E. M., Kokudo, N., Miyazaki, M., and Pawlik, T. M. (2015). Intrahepatic cholangiocarcinoma: Expert consensus statement. *HPB Oxf.* 17, 669–680. doi:10.1111/hpb.12441

Wei, H., Gao, L., Fan, K., Liu, J., He, J., Qu, X., et al. (2021). Nanozymes: A clear definition with fuzzy edges. *Nano Today* 40, 101269. doi:10.1016/j.nantod.2021.101269

Wojtkowiak, J. W., Verduzco, D., Schramm, K. J., and Gillies, R. J. (2011). Drug resistance and cellular adaptation to tumor acidic pH microenvironment. *Mol. Pharm.* 8, 2032–2038. doi:10.1021/mp200292c

Wu, H., Liu, L., Song, L., Ma, M., Gu, N., and Zhang, Y. (2019). Enhanced tumor synergistic therapy by injectable magnetic hydrogel mediated generation of hyperthermia and highly toxic reactive oxygen species. *ACS Nano* 13, 14013–14023. doi:10.1021/acsnano.9b06134

Xu, X. F., Xing, H., Han, J., Li, Z. L., Lau, W. Y., Zhou, Y. H., et al. (2019). Risk factors, patterns, and outcomes of late recurrence after liver resection for hepatocellular carcinoma: A multicenter study from China. *JAMA Surg.* 154, 209–217. doi:10.1001/jamasurg.2018.4334

Xu, G., Du, X., Wang, W., Qu, Y., Liu, X., Zhao, M., et al. (2022a). Plasmonic nanozymes: Leveraging localized surface plasmon resonance to boost the enzyme-mimicking activity of nanomaterials. *Small* 18, e2204131. doi:10.1002/smll.202204131

Xu, Z., Chen, J., Li, Y., Hu, T., Fan, L., XI, J., et al. (2022b). Yolk-shell Fe(3)O(4)@Carbon@Platinum-Chlorin e6 nanozyme for MRI-assisted synergistic catalytic-photodynamic-photothermal tumor therapy. *J. Colloid Interface Sci.* 628, 1033–1043. doi:10.1016/j.jcis.2022.08.006

Yang, J. D., Hainaut, P., Gores, G. J., Amadou, A., Plymoth, A., and Roberts, L. R. (2019). A global view of hepatocellular carcinoma: Trends, risk, prevention and management. *Nat. Rev. Gastroenterol. Hepatol.* 16, 589–604. doi:10.1038/s41575-019-0186-y

Yoon, H. I., and Seong, J. (2014). Multimodality treatment involving radiotherapy for advanced liver-confined hepatocellular carcinoma. *Oncology* 87 (1), 90–98. doi:10.1159/000368151

Zandieh, M., and Liu, J. (2021). Nanozyme catalytic turnover and self-limited reactions. *ACS Nano* 15, 15645–15655. doi:10.1021/acsnano.1c07520

Zeng, J., Goldfeld, D., and Xia, Y. (2013). A plasmon-assisted optofluidic (PAOF) system for measuring the photothermal conversion efficiencies of gold nanostructures and controlling an electrical switch. *Angew. Chem. Int. Ed. Engl.* 52, 4263–4267. doi:10.1002/ange.201210359

Zhang, C., Bu, W., Ni, D., Zhang, S., Li, Q., Yao, Z., et al. (2016). Synthesis of iron nanometallic glasses and their application in cancer therapy by a localized Fenton reaction. *Angew. Chem. Int. Ed. Engl.* 55, 2141–2146. doi:10.1002/ange.201510031

Zhang, B., Hu, X., Jia, Y., Li, J., and Zhao, Z. (2021a). Polyaniline@Au organic-inorganic nanohybrids with thermometer readout for photothermal immunoassay of tumor marker. *Mikrochim. Acta* 188, 63. doi:10.1007/s00604-021-04719-y

Zhang, Y., Yang, Y., Shi, J., and Wang, L. (2021b). A multimodal strategy of Fe(3)O(4)@ZIF-8/GOx@MnO(2) hybrid nanozyme via TME modulation for tumor therapy. *Nanoscale* 13, 16571–16588. doi:10.1039/d1nr04196g

Zhao, P., Jiang, Y., Tang, Z., Li, Y., Sun, B., Wu, Y., et al. (2021). Constructing electron levers in perovskite nanocrystals to regulate the local electron density for intensive chemodynamic therapy. *Angew. Chem. Int. Ed. Engl.* 60, 8987–8994. doi:10.1002/ange.202100864

Zhu, Z. X., Huang, J. W., Liao, M. H., and Zeng, Y. (2016). Treatment strategy for hepatocellular carcinoma in China: Radiofrequency ablation versus liver resection. *Jpn. J. Clin. Oncol.* 46, 1075–1080. doi:10.1093/jjco/hyw134

Zhu, Y., Wang, Z., Zhao, R., Zhou, Y., Feng, L., Gai, S., et al. (2022). Pt decorated $Ti_3C_2T_x$ MXene with NIR-II light amplified nanozyme catalytic activity for efficient phototheranostics. *ACS Nano* 16, 3105–3118. doi:10.1021/acsnano.1c10732

Zuo, W., Fan, Z., Chen, L., Liu, J., Wan, Z., Xiao, Z., et al. (2022). Copper-based theranostic nanocatalysts for synergetic photothermal-chemodynamic therapy. *Acta Biomater.* 147, 258–269. doi:10.1016/j.actbio.2022.05.030